CHEMISTRY OF MATERIALS

Article

pubs.acs.org/cm

Novel Near-Room-Temperature Type I Multiferroic: $Pb(Fe_{0.5}Ti_{0.25}W_{0.25})O_3$ with Coexistence of Ferroelectricity and Weak Ferromagnetism

Sebastián A. Larrégola,*[,†] José C. Pedregosa,[†] Miguel Algueró,[‡] Ricardo Jiménez,[‡] Mar García-Hernandez,[‡] María T. Fernández-Díaz,[§] and José A. Alonso[‡]

[†]INTEQUI-Área de Química General e Inorgánica "Dr. Gabino F. Puelles", Departamento de Química, Facultad de Química, Bioquímica y Farmacia, Universidad Nacional de San Luis, Chacabuco y Pedernera, 5700 San Luis, Argentina

[‡]Instituto de Ciencia de Materiales de Madrid, C.S.I.C., Cantoblanco, 28049 Madrid, Spain

[§]Institut Max Von Laue Paul Langevin, F-38042 Grenoble, France

Supporting Information

ABSTRACT: We report on the crystal structure evolution and the physical properties of the complex perovskite $Pb(Fe_{0.5}Ti_{0.25}W_{0.25})O_3$. It presents a paraelectric to ferroelectric transition at T_C = 293 K, determined by permittivity measurements. The room-temperature neutron powder diffraction pattern (NPD) shows an admixture of the ferroelectric phase (34%, *P4mm* space group) and the paraelectric polymorph (66%, $Pm\bar{3}m$ space group). In both polymorphs, the perovskite crystal structure contains the three B cations (Fe, Ti, W) distributed at random at the octahedral sites, and Pb is shifted away from the center of the cubic (sub)cell. On the other hand, the presence of iron drives the appearance of magnetic interactions above room temperature. This is related to the existence of Fe-rich islands where the strong Fe^{3+}−O−Fe^{3+} superexchange interactions govern the magnetic behavior. The magnetic structure has been determined from low-temperature NPD experiments as a G-type antiferromagnetic (AFM) cell. Furthermore, there is a net magnetization in the entire range of temperature, which is related to the existence of noncompensated spins in each island. The coexistence of ferroelectricity and a magnetically ordered system and the observation of a possible coupling between both phenomena allow us to suggest the multiferroic-magnetoelectric nature of the sample.

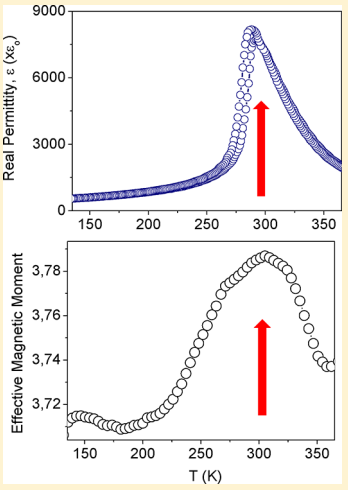

KEYWORDS: *perovskite, ferroelectric, multiferroic, magnetoelectric, lead*

INTRODUCTION

Multifunctional systems are appealing for materials researchers, due to the great number of technological and fundamental opportunities that they present. An important type is constituted by the well-known ferromagnetic-ferroelectrics or multiferroic-magnetoelectrics, which allow the magnetic control of electric polarization and vice versa, generating applications as novel random access memories, in which an electric field switches the magnetization (electrical-writing) due to the interaction that exists between both phenomena (magneto-electric coupling), while standard magnetic reading is implemented.[1]

The design of multifunctional materials is rather complex because both properties call for a different type of requirements. On one hand, the presence of ferromagnetism requires the existence of unpaired d-electrons (for instance in $(La,Sr)MnO_3$), whereas the ferroelectricity (e.g., in $BaTiO_3$) is generated by the off-centering of the Ti(IV) cation driven by the existence of a strong hybridization between the metal d^0-states with the occupied oxide p-states;[2,3] this kind of distortion is called second-order Jahn−Teller effect (SOJT). In this way, it is commonly accepted that ferroelectricity only appears in non-centrosymmetric crystal structures, or polar nanoregions in the case of relaxor type ferroelectrics,[4] while magnetic cations tend to adopt highly symmetric coordination environments. This fact originates an incompatibility between both types of ferroic behaviors, justifying the difficulties observed in the design and synthesis of these multifunctional materials.[5]

However, there are diverse strategies that have been developed to avoid the mentioned incompatibilities; the most commonly used consists of decoupling the centers responsible of ferroelectricity and ferromagnetism, by the incorporation of different ions able to induce both kinds of orderings.[6−10] The perovskite-type compounds are, for instance, a very good starting point to perform the design of new multiferroic materials because they have an enormous versatility to include different type of cations in the lattice, such as first-row transition metals at the B positions and p-block lone-pair

Received: February 11, 2012
Revised: June 11, 2012

   dx.doi.org/10.1021/cm300470f | *Chem. Mater.* XXXX, XXX, XXX−XXX

elements at the A perovskite sublattice. In these samples, the ns^2 lone pair acquires a polarization in a specific way, due to the presence of a strong hybridization between the s- and p-states of the cation with the oxygen p-states, giving rise to local asymmetries and thus to ferroelectric or antiferroelectric polarizations.[11,12] An alternative strategy consists of designing perovskites including a solid solution at the B positions, by the incorporation of a second asymmetry seed, related with the replacement of a fraction of the magnetic atom with a d^0-ferroactive ion, like Nb(V) in $Pb(Fe_{1/2}Nb_{1/2})O_3$[13−15] or W(VI) in $Pb(Fe_{2/3}W_{1/3})O_3$.[16]

Promising candidates in the search of multiferroic materials could be some derivatives of the perovskite $BiMnO_3$,[17] or the highly distorted perovskites $(In/Mn)(Fe,Mn)O_3$ reported by Belik et al.,[18] which present a ferromagnetic ordering below 100 K, and a proposed, yet not experimentally demonstrated, ferroelectric character at room temperature; however, these compounds can be only obtained by using a high pressure and high temperature synthesis technique. Another possibility is to find new perovskites derived from $PbTiO_3$[19] in which, through appropriate substitutions including magnetic ions, the induction of magnetoelectric properties can be achieved. Following this pathway and the strategies specified in the precedent paragraph, we have designed and synthesized a perovskite of formula $Pb(Fe_{0.5}Ti_{0.25}W_{0.25})O_3$, with potential multiferroic behavior. The crystal structure evolution of this sample has been investigated by neutron powder diffraction (NPD) data between 2 K and room temperature (RT); the study of macroscopic magnetization and dielectric permittivity shows a very interesting behavior due to the combination of magnetic (d^n) and ferroactive (d^0) ions at the B sublattice of the perovskite, accompanied by the presence of a lone pair element (Pb(II)) at the A sublattice.

EXPERIMENTAL SECTION

$Pb(Fe_{0.5}Ti_{0.25}W_{0.25})O_3$ (PFTW) was prepared by standard solid-state techniques; as starting materials PbO (CERAC 99.99%), Fe_2O_3 (Strem chemicals 99.99%), TiO_2 (Strem chemicals 99.99%), and WO_3 (Merck 99.9%) were used. They were weighed out in the appropriate metal ratios and well mixed in an agate mortar. The mixture was calcined at 600 °C in two steps of 12 h with intermediate grindings. Subsequently, the product was heated at 800 °C for 24 h and finally at 900 °C for 12 h until a single phase was obtained. All the thermal treatments were carried out in sintered alumina crucibles and in air atmosphere, and no weight losses were observed from the starting reagents. PFTW was obtained as a well-crystallized dark red powder.

Sample characterization was performed by X-ray powder diffraction (XRPD) measurements using a Bruker-AXS D8 diffractometer (40 kV, 30 mA), controlled by DIFFRACT Plus software, in Bragg−Brentano reflection geometry with Cu Kα radiation (λ = 1.5418 Å). A secondary graphite monochromator allowed the complete removal of Cu Kβ radiation. The data were obtained between 10 and 70° (2θ scans) in steps of 0.05°.

Neutron powder diffraction data were collected on the high resolution powder diffractometer D2B (λ = 1.594 Å) at room temperature and on the D20 diffractometer (λ = 2.41 Å) in a range of temperatures between 2 and 296 K, at the Institut Laue-Langevin (ILL), Grenoble, France. The powder sample was contained in a vanadium cylinder. The refinement of the crystal and magnetic structures was performed by the Rietveld method, using the FULLPROF refinement program.[20] A pseudo-Voigt function was chosen to fit the diffraction peak shapes. The following parameters were refined in the final run of the D2B high resolution data set: scale factor, background coefficients, zero point error, pseudo-Voigt peak shape function corrected for asymmetry, positional coordinates, and isotropic thermal factors. For the sequential refinement from the data set collected in D20, the z component of the magnetic moments localized on the B-site atoms, the unit cell parameters, and the atomic coordinates were also refined.

The magnetic measurements were performed in a commercial superconducting quantum interference device magnetometer (SQUID). The dc magnetic susceptibility data were collected in the $5 < T < 400$ K range, under an applied magnetic field of 1000 Oe. Isothermal magnetization curves were obtained for magnetic fields going from −5 to 5 T at 2, 150, and 350 K.

For the electrical characterization, ceramic disk samples were processed by conventional sintering at 900 °C, thinned and electroded with Ag paint (firing at 250 °C). The temperature dependence of the dielectric permittivity was measured below RT down to 77 K with a HP4284A precision LCR meter. Measurements were dynamically carried out during a heating−cooling cycle from the liquid nitrogen temperature at ±1.5 K min^{-1}, and at several frequencies between 0.1 kHz and 1000 kHz.

Ferroelectric loops were also characterized in the same temperature range. Low-frequency (0.1−10 Hz), high-voltage (up to 10 kV) sine waves were applied by the combination of a synthesizer/function generator (HP 3325B) and a high voltage amplifier (Trek model 10/40A), and charge was measured with home-built charge to voltage converter and software for loop acquisition and analysis.

RESULTS

Structural Determination at RT. The XRPD pattern of PFTW obtained at RT, typical of a perovskite structure, is shown in Figure 1. No superstructure reflections were observed

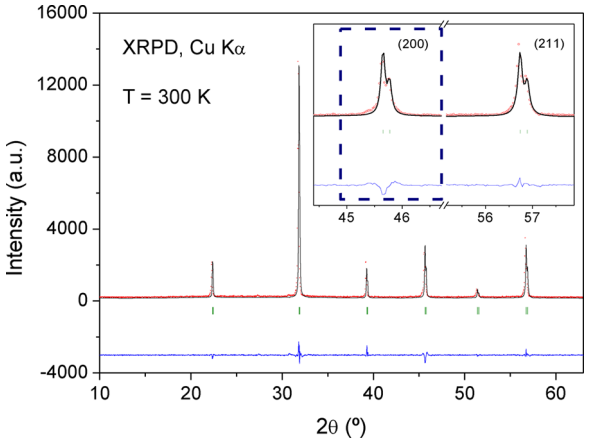

Figure 1. Rietveld fit from X-ray powder diffraction data of a conventional cubic ($a \approx 4$ Å) perovskite structure. The inset shows the poor resolution obtained for the (200) reflection.

in this pattern; as a first approximation, it has been indexed in the cubic system, space group $Pm\bar{3}m$ (no. 223), with a unit-cell parameter $a \approx 4$ Å. Figure 1 illustrates an acceptable Rietveld fit using this model. However, a closer analysis of several regions of the refinement shows that some reflections are broadened (see the inset of Figure 1, first related to the [200] reflection), which cannot be solved with the proposed crystallographic model.

To go deeply in the understanding of this system, we have performed a neutron diffraction study at room temperature. Figure S1a (Supporting Information) shows that after the refinement using a simple cubic structure the mentioned widening is more pronounced and not solved by the model, as illustrated in Figure S1b−d in the Supporting Information. This fact could be related to a paraelectric to ferroelectric phase transition (PE−FE) revealed by the permittivity measurements

dx.doi.org/10.1021/cm300470f | Chem. Mater. XXXX, XXX, XXX−XXX

(see the next section), and could be associated with a phase coexistence of a cubic-paraelectric polymorph and polar (non-centrosymmetric) polymorph, since the phase transition occurs near RT.

We have analyzed different possible symmetries that could be adopted by the second polymorph, using three of the most commonly observed ferroelectric perovskite structures: the rhombohedral *R*3*c* and *R*3*m* structures and the tetragonal *P*4*mm* one. From several Rietveld refinements, the system where the cubic (α polymorph, P_α) and the tetragonal *P*4*mm* structure (β polymorph, P_β) coexist yields the best fit.

The model of the cubic polymorph is the typically observed in simple perovskites, where the three B-cations are located at the same crystallographic 1a Wyckoff sites (000), Pb atoms at 1b positions ($^1/_2$ $^1/_2$ $^1/_2$) and O atoms at the 3d-sites ($^1/_2$ 0 0). On the other hand, in the tetragonal *P*4*mm* cell, it is necessary to define two types of crystallographically nonequivalent oxygen atoms; one located at the ($^1/_2$ $^1/_2$ *z*) position and the second at ($^1/_2$ 0 *z*). Lead atoms are placed at 1a sites (0 0 *z*) while the B cations at ($^1/_2$ $^1/_2$ *z*). In the later structure, all the atoms present a variable *z*-coordinate, suggesting the presence of atomic displacements along the *c*-axis of the unit cell; this fact gives rise to the polar nature of the β-polymorph crystal structure. From the refinement of the scale factors at RT, there is a coexistence of a major cubic polymorph (66(4)%) and a minor tetragonal phase (34(4)%). In this two-phase model, all the reflections are correctly solved, as shown in Figure 2. Table I lists the unit-cell parameters, atomic positions, isotropic thermal factors, and reliability factors of the refinement including both polymorphic phases, and Table II contains the main bond lengths and some selected bond angles.

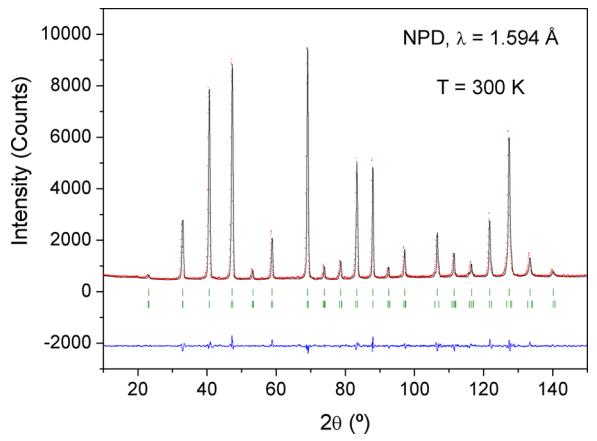

Figure 2. Two phases Rietveld refinement from NPD data at RT for a mixture of a main cubic *Pm*$\bar{3}$*m* polymorph and a tetragonal *P*4*mm* polymorph.

Dielectric Permittivity Measurements. The dynamic measurements performed as a function of temperature on a sintered pellet of PFTW are shown in Figure 3a; additionally several curves collected at different frequencies are displayed in Figure S.2 in the Supporting Information. These curves exhibit a well-defined, sharp maximum in the real part of the permittivity, at 293 K approximately, showing a marked thermal hysteresis ($\Delta T \approx 13$ K) and whose position does not shift with the applied frequency. This fact is in agreement with the presence of a paraelectric-to-ferroelectric (PE–FE) macroscopic phase transition near RT. Note the presence of a large dielectric dispersion from 175 K, which is usually indicative of the triggering of conduction. The evolution of the reciprocal permittivity is shown in Figure S.3 in the Supporting Information as dots, and a Curie–Weiss fitting in the paraelectric phase is represented by a full red line. From this

Table I. Unit Cell Parameters, Positional and Displacement Parameters, Isotropic Thermal Factors, and Reliability Factors for both P_α and P_β, from NPD at 295 K

param.	P_α (*Pm*$\bar{3}$*m*)	P_β (*P*4*mm*)
$a = b$ (Å)	3.9762(1)	3.9648(2)
c (Å)	= a	3.9933(3)
volume	62.865(4)	62.774(6)
c/a	1	1.007
	Pb Environment	
x	0.471(2)	0
y	0.471(2)	0
z	0.471(2)	0.613(3)
B_{iso} (Å^2)	0.91(5)	1.2(3)
	B Environment	
x	0	0.5
y	0	0.5
z	0	0.084(4)
B_{iso} (Å^2)	0.14(4)	1.32(5)
	O1 Environment	
x	0	0.5
y	0.5	0.5
z	0	0.555(4)
B_{iso} (Å^2)	0.78(4)	1.92(2)
	O2 Environment	
x		0.5
y		0
z		0.048(2)
B_{iso} (Å^2)		1.57(2)
% phase	66(2)	34(2)
	Reliability Factors	
R_{Bragg}	1.90	2.54
R_p (%)	8.32	
R_{wp} (%)	8.11	
R_{exp} (%)	3.91	
χ^2	4.30	

Table II. Main Interatomic Distances (Å) and Angles (deg) Obtained for Both Polymorphic Phases from the NPD Data Refinement at 295 K

	P_α (*Pm*$\bar{3}$*m*)	P_β (*P*4*mm*)
	PbO_{12}	
Pb–O (1)	6 × 2.815(1)	4 × 2.6351(1)
Pb–O (1)	3 × 2.642(1)	4 × 3.0042(1)
Pb–O (T 2)	3 × 2.979(1)	4 × 2.8132(1)
⟨Pb–O⟩	2.8127	2.8175
δ_{Pb}	0.21	0.452(3)
	BO_6	
	Bond Lengths	
B–O	6 × 1.9881(1)	4 × 1.9877(8)
B–O		1.8795(1)
0.5		2.1138(1)
⟨B–O⟩	1.9881	1.9907
δ_B	0	0.234(3)
	Bond Angles	
O1–B–O1	180.0	180.0
O1–B–O2	90.0	94.2(3)
O2–B–O2	180.0	171.6(2)

dx.doi.org/10.1021/cm300470f | *Chem. Mater.* XXXX, XXX, XXX–XXX

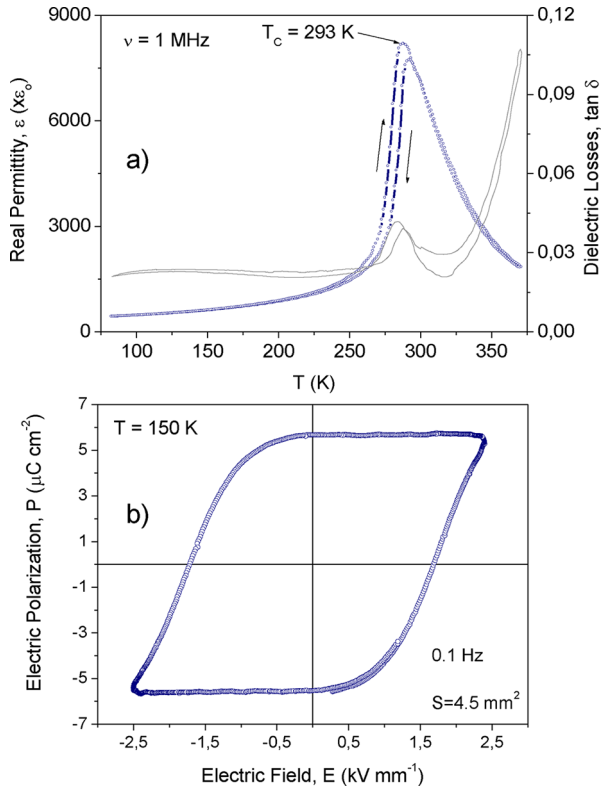

Figure 3. (a) Temperature dependence of the real permittivity (full line) and dielectric losses (dotted line) of PFTW collected at 1 MHz. The arrows indicate the temperature progression. (b) Electric polarization as a function of the applied electric field, showing a hysteresis loop obtained at 150 K with an external frequency of 0.1 Hz.

fit, a Curie–Weiss constant of 1.376×10^{-5} K was obtained, in the typical range for displacive ferroelectric transitions and very close to that of $BaTiO_3$.[21] The Curie–Weiss temperature was T_C = 297.3 K, which is higher than the temperature of the dielectric maximum. This indicates that the FE tetragonal phase exists at temperatures above the maximum, most probably up to 330 K, temperature at which the reciprocal permittivity deviates from the Curie–Weiss behavior. This somehow resembles the behavior of materials showing a relaxor to ferroelectric transition, such as 0.65 $Pb(Mg_{1/3}Nb_{2/3})O_3$–0.35 $PbTiO_3$,[22] for which polar nanoregions start nucleating at temperatures well above the transition temperature. The ferroelectric nature of the low temperature structure was confirmed by the measurement of a hysteresis loop at 150 K. This is plotted in Figure 3b and presents a remnant polarization of ±5.7 $\mu C/cm^2$ and a coercive field that reaches the value of 1.7 kV/mm at 2.5 kV/mm maximum field.

Following of the Phase Transition and Magnetic Structure at Low Temperatures. Given the proximity of the paraelectric to ferroelectric phase transition to RT ($T_C \approx 293$ K) in our PFTW oxide, we have an admixture of both polymorphs in the NPD pattern at RT. The phase transition sequence *P4mm* (low-temperature polymorph) → *Pm*$\bar{3}$*m* (high-temperature polymorph) is that previously reported for the paradigmatic example of $PbTiO_3$.[23]

The structural evolution has been followed from sequential NPD data in the 2–296 K range. Figure 4a shows a tridimensional plot of the neutron diffraction patterns collected at D20 in this temperature range. Despite the longer wavelength used in D20 (λ = 2.41 Å), allowing us accessing to a reduced number of reflections, the study of the crystal structure evolution could be performed without significant problems given the high symmetry of both phases. Certain reflections, such as the $(200)_{cubic}$ around $2\theta \approx 75°$, undergo a strong reorganization upon the phase transition.

Figure 4b shows the thermal evolution of two reflections: the $(111)_{cubic}$ shows no widening or splitting in the entire range of temperature, supporting in this way the selection of the tetragonal model instead the rhombohedral ones, in which the mentioned cubic reflection should split into two components (006) and (202) upon the transition to the low-temperature

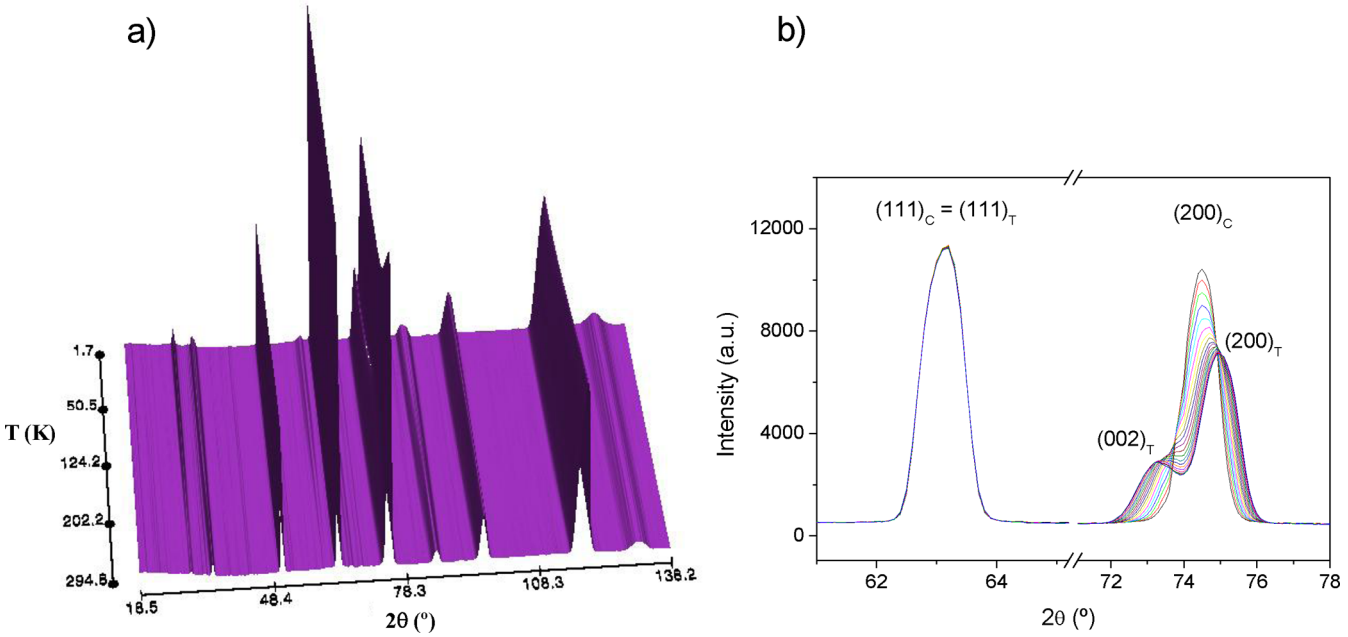

Figure 4. (a) Thermal progression of the neutron powder diffraction patterns collected at D20 from 2 to 296 K. (b) Temperature evolution of the (111) and (200) cubic reflections.

dx.doi.org/10.1021/cm300470f | Chem. Mater. XXXX, XXX, XXX–XXX

polar polymorph. Moreover, the choice of the tetragonal model is sustained by the splitting observed for the $(200)_{cubic}$ reflection into two components, the $(200)_{tetra}$ and the $(002)_{tetra}$, in agreement with the appearance of an expansion along the *c*-axis and a contraction of the *ab*-plane. From the analysis of the splitting model, no evidence of interoctahedral tilting was observed, which is in agreement with the proposed tetragonal model.

On the other hand, the phase transition is accompanied by the development of two tiny peaks at $2\theta = 30°$ ($d_1 = 4.56$ Å) and $2\theta = 60°$ ($d_2 = 2.38$ Å), which grow in intensity as temperature decreases; these peaks are independent of the crystal structure reflections. This fact is related to the development of a long-range magnetic ordering, probably consisting of an antiferromagnetic structure. Figure S.4, Supporting Information, shows a zoom of the low-angle region: the magnetic peaks have nonzero intensity even at room temperature, suggesting that $T_N > 296$ K. The magnetic structure has been modeled as a G-type AFM cell, based on the tetragonal *P4mm* polymorph, which is characterized by a propagation vector $k = [^1/_2\ ^1/_2\ ^1/_2]$, in which the magnetic moments situated on the Fe(III) cations are oriented parallel to the *c*-axis and they are antiferromagnetically coupled to the six nearest neighbors (disregarding, so far, the cationic disorder). The evolution of the crystal and magnetic structures has been investigated by sequentially refining the NPD patterns from 2 to 296 K. Figure 5 illustrates the fit of the pattern collected at 2 K, where observed and calculated patterns are in excellent agreement for the proposed model.

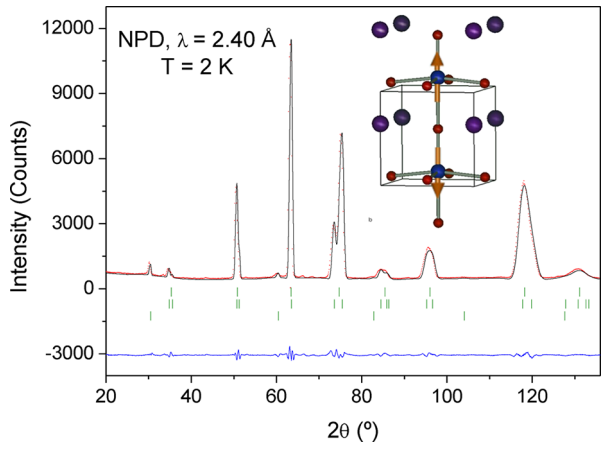

Figure 5. Observed (crosses), calculated (full line), and difference (below) NPD patterns at 2K after the Rietveld refinement of the crystal and magnetic structures of PFTW. The first and second lines of reflections represent the cubic and tetragonal polymorphic phases, whereas the third line represents the magnetic cell. The inset shows the magnetic structure model (G-type) used in the refinement.

Figure 6 shows the thermal evolution of the unit-cell parameters (Figure 6a), the tetragonality index (Figure 6b), and the fraction of each polymorph between RT and 2 K (Figure 6c). The composition of the phase admixture varies notably from RT to low temperatures, in agreement with the presence of a phase transition, showing two different zones: The first one is the cubic or paraelectric zone where the alpha polymorph rules the structure and properties of the perovskite. Then, at temperatures lower than 293 K the tetragonal polymorph is the most stable structure and the sample becomes ferroelectric. It is

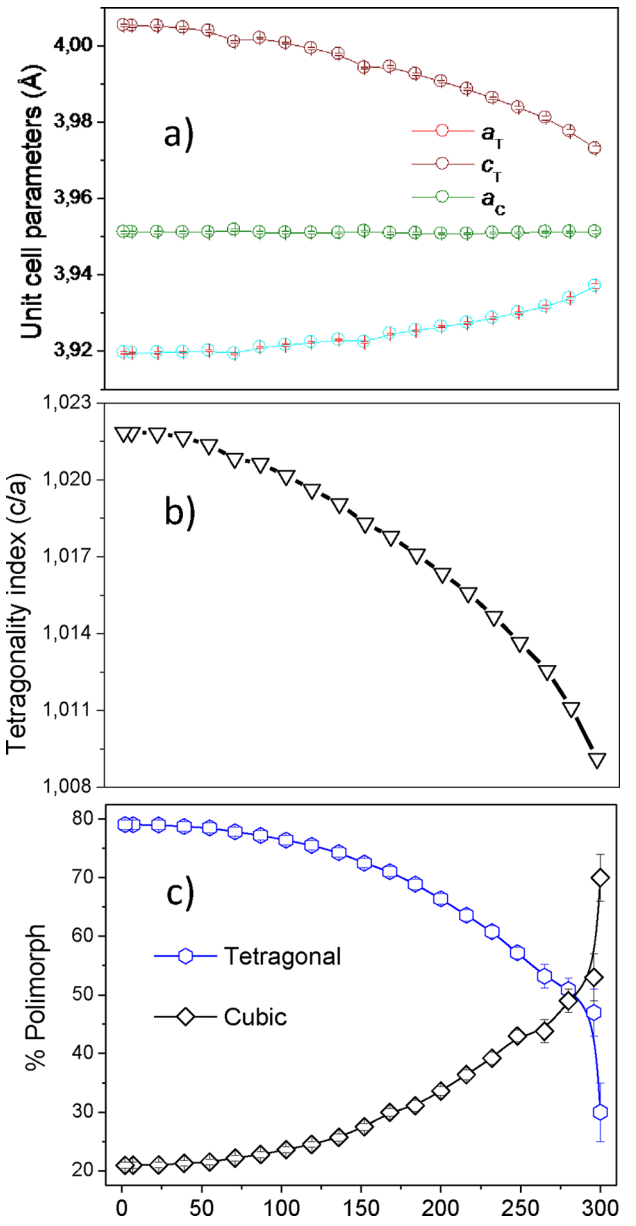

Figure 6. (a) Thermal evolution of the unit-cell parameters obtained for both polymorphic structures: a_T and c_T represent the tetragonal parameters, while a_C is referred to the cubic parameter. (b) Thermal evolution of the tetragonality index defined as $t = c_T/a_T$. (c) Dependence of the percentage of each polymorph with temperature: The blue line represents the concentration of the tetragonal phase and the black one the corresponding to the cubic sample.

remarkable that both polymorphic phases coexist in the entire range of temperature, from the transition temperature down to 2 K, which is quite an unexpected behavior for a conventional ferroelectric transition. We will come back to this issue in the Discussion.

The evolution of the cubic unit-cell parameter shows a little and steady contraction as temperature diminishes, while the tetragonal polymorph displays a contraction of the *a* (=*b*) parameter and an expansion of the *c* parameter. The contraction of the *ab* plane and the expansion along the *c*-axis implies an enhancement of the tetragonal distortion of the structure (tetragonality index, defined as $t = a_T/c_T$), which is due to the antiparallel shifting (on the c direction) of both

dx.doi.org/10.1021/cm300470f | *Chem. Mater.* XXXX, XXX, XXX–XXX

cationic sublattices in respect to the anionic one. At 2 K the tetragonality index reaches a value of 1.022 (see Figure 6b).

Magnetic Measurements. The thermal evolution of the magnetic susceptibility for $Pb(Fe_{0.5}Ti_{0.25}W_{0.25})O_3$ is displayed in Figure 7a. The susceptibility increases upon cooling, showing

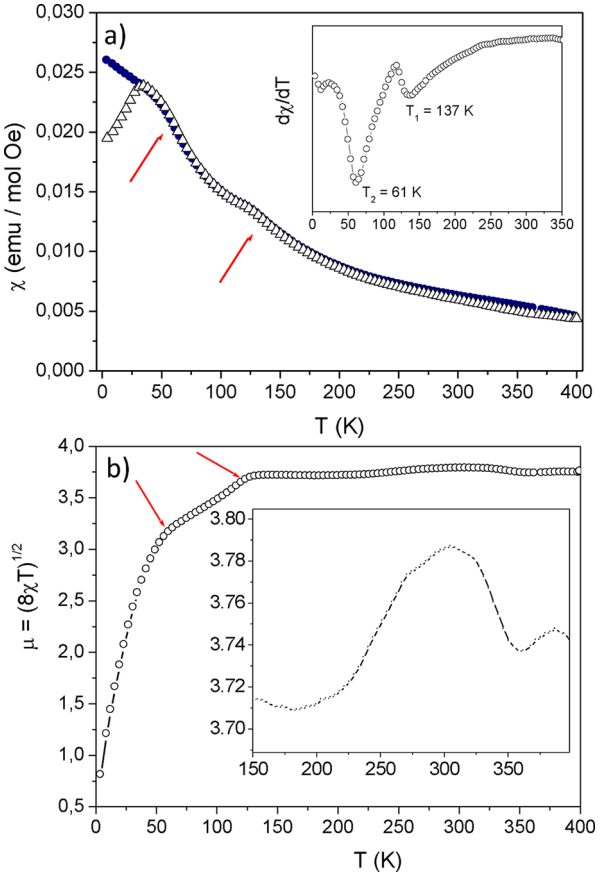

Figure 7. (a) Thermal evolution of the magnetic susceptibility: field cooling (blue circles) and zero field cooling (black triangles). The inset shows the derivative curve of the susceptibility. (b) Thermal evolution of the effective magnetic moment obtained as $\mu_{eff} = \sqrt{(8\chi T)}$. Red arrows indicate the magnetic events.

two anomalies signaled with arrows. The inset shows the susceptibility derivative curve, where the mentioned magnetic events are localized at 137 and 61 K. In addition, we have observed no Curie–Weiss behavior in the entire range of temperature, in agreement with the presence of magnetic peaks at room temperature in the NPD patterns. Finally, both FC and ZFC curves present a separation at temperatures lower than 30 K, which could be related to the development of some kind of freezing phenomenon giving rise to a spin glass or a cluster glass state.

The nature of the magnetic events can be understood from the analysis of the thermal evolution of the effective magnetic moment, calculated as $\mu_{eff} = \sqrt{8\chi T}$. This one is plotted at Figure 7b, and the previously remarked magnetic events are related to abrupt drops of the paramagnetic moment and thus of the long-range antiferromagnetic ordering of the spins.

On the other hand, Figure 8 shows three isothermal magnetization curves collected at 350, 150, and 2 K. From these data, it is possible to observe the presence of a tiny hysteresis loop at 350 K with a little coercive field (200 Oe). At 150 K, the magnitude of the coercive field presents a little

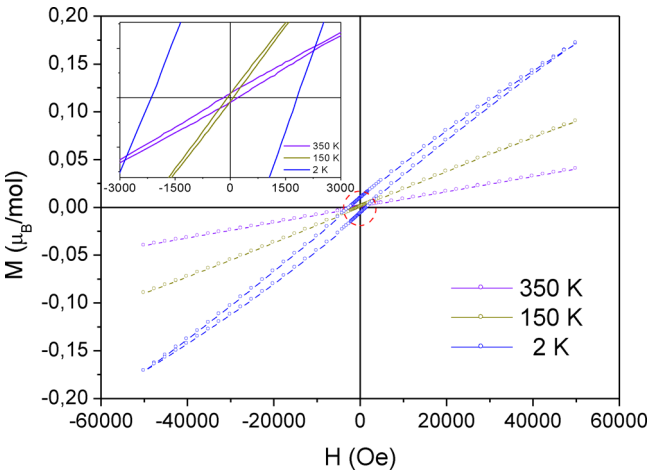

Figure 8. Isothermal magnetization curves measured at 2, 150, and 350 K for PFTW.

decrease (80 Oe). However, the loop collected at 2 K shows an important increase of the coercive field (1800 Oe) and the remnant magnetization, suggesting the presence of a possible canting in the antiferromagnetically coupled magnetic moments.

DISCUSSION

From the structural Rietveld refinement performed at RT, two polymorphic phases were observed. The cubic paraelectric one (66(4)%) presents a disorder of the lead atoms typically observed in lead-based perovskites. We have modeled this disorder and have found the existence of a 0.21 Å shift from the center of the polyhedron along the [111] cubic direction of the unit cell. Additionally, the B cations (Fe, Ti, W) are distributed at random at the same crystallographic site, which gives rise to a solid solution at these positions. Finally, we have checked the possible presence of oxygen and lead vacancies, and no deviation from the nominal stoichiometry was observed within the experimental error.

The tetragonal polymorph is defined in a polar (non-centrosymmetric) space group. The defined distortion is related to several cationic shifts, and there is no evidence of octahedral tilting. The crystal structure of the tetragonal polymorph is characterized by an expansion of the *c* axis and a compression of the *ab*-plane with respect to the cubic phase. At room temperature, the tetragonal distortion is very subtle, showing a tetragonality index ($t = c/a$) of 1.007, while the observed for the isostructural $PbTiO_3$ is of about 1.06 at RT.[23] However, it is important to remark that the FE phase of $PbTiO_3$ is stable up to the Curie temperature of 763 K, whereas the present PFTW phase shows a Curie point of roughly 300 K. In relation to the nature of the phase transition, the existence of thermal hysteresis in the transition temperature and the coexistence of both polymorphs in this temperature range suggest it to be first order. However, the Curie temperature higher than the transition temperature, the loss of the Curie–Weiss behavior from a temperature 40 K above the transition temperature, and mainly, the persistence of significant levels of the cubic paraelectric phase down to 2 K indicate that this is not the case.

Coming back to the crystal structure of this polymorph, detailed in Figure 9, it is interesting to note that the expansion of the *c*-axis is linked to relative shifts of both the anionic (O^{2-}) and cationic sublattices along the mentioned direction. As a

dx.doi.org/10.1021/cm300470f | Chem. Mater. XXXX, XXX, XXX–XXX

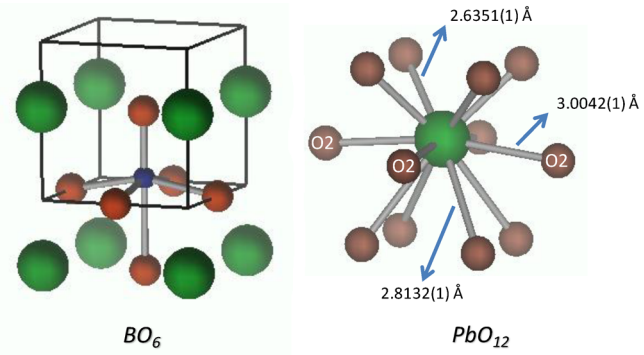

Figure 9. Schematic representation of the crystal structure of the tetragonal polymorph under study. The left panel details the octahedral distortion of the B cation and the right panel shows the lead coordination polyhedron.

result, the A and B cations are shifted from the center of the respective polyhedra, as follows. Lead atoms show an off-centering of 0.452 Å along the [001] direction. As a consequence, there are three groups of Pb−O bond lengths, which are detailed in Table II. There are four long Pb−O1 distances, four intermediate Pb−O2 ones, and four short Pb−O1 bond lengths. An additional cationic off-centering is observed for the B-site atoms, which are displaced from the center of the octahedron along the C1 local-direction, which is the same as the [001] one. This shift emphasizes the dipolar moment present at the unit cell of the ferroelectric polymorph, and guides the B cations to an ideal square pyramidal coordination. However, in this case, the magnitude of the shift is smaller, taking the value of 0.234 Å, maintaining a distorted octahedral coordination. On the other hand, several isostructural compounds have previously been reported, such as $BiCoO_3$[24] oxide, which shows a pentagonal coordination of the cobalt cations, as a result of the presence of a severe tetragonal distortion (room-temperature tetragonality index $t = 1.267$).

To evaluate the octahedral distortion, the Δd parameter has been calculated, as defined by Halasyamani:[25]

$$\Delta d = \frac{\|(M-\mathrm{O1})-(M-\mathrm{O2})\|}{\|\cos\langle \mathrm{O1}-M-\mathrm{O2}\rangle\|} + \frac{\|(M-\mathrm{O3})-(M-\mathrm{O4})\|}{\|\cos\langle \mathrm{O3}-M-\mathrm{O4}\rangle\|} + \frac{\|(M-\mathrm{O5})-(M-\mathrm{O6})\|}{\|\cos\langle \mathrm{O5}-M-\mathrm{O6}\rangle\|}$$

where the pairs (O1,O2), (O3,O4), and (O5,O6) are the oxygen atoms that constitute the octahedron and are located in opposite positions from each other. The obtained value for the BO_6 octahedron in PFTW is $\Delta d = 0.234$, and it falls into the first category defined by Halasyamani,[25] with a magnitude located in the range of $0.05 < \Delta d < 0.4$; following the criteria proposed by the author, this figure corresponds to a weak magnitude of octahedral distortion.

This kind of distortion has been rationalized by ab initio studies using density functional theory (DFT) methods, and it is related with the presence of transition metal ions with d^0 electronic configuration, which suffers a second-order Jahn−Teller distortion.[26] This effect occurs, in the case of ions in octahedral coordination, when the empty d-orbitals of the metal are mixed with the p-states of the oxide ligands. In extended structures, this mixture results in a great number of degenerated electronic configurations, which can be removed by the appearance of a spontaneous shift of the metal from the center of its polyhedron in a particular crystallographic direction.

Taking this fact into account, it is important to remark that the sample presents three different types of cations (Fe^{3+} ($3d^5$), Ti^{4+} ($3d^0$), and W^{6+} ($5d^0$)), randomly located at the B sublattice. In fact, Ti and W cations present a marked ferroactive character driven by the small ionic radii and the d^0 electronic configuration. Moreover, as Fe atoms are d^5 cations, in high spin configuration there is no crystal field stabilization for any particular geometry and the coordination environment could be quite distorted, as it occurs in $BiFeO_3$.[27] In fact, the presence of three different cations at the octahedral sites and the different tendencies to exhibit SOJT effects, could be in the origin of the high value of the isotropic thermal factor ($B_{iso} = 1.2(3)$ Å^2) obtained from the NPD refinement at RT, suggesting that there is a small disorder in the shifting pattern of the three different cations. In order to get a deeper description of the local environments of the B-site cations, EXAFS experiments should be carried out.

All of these data derived from the crystallographic analysis are in agreement with the dielectric measurements, which present an intense peak in the real part of the permittivity, independently of the applied frequency. Moreover, a clear ferroelectric hysteresis loop has been recorded at 150 K confirming the ferroelectric nature of the β-polymorph. The calculation of the expected polarization from the atomic displacements, taking into account the nominal ionic charges, was carried out by using the equation:

$$P_S = V^{-1}\sum \mathrm{Ze}\delta$$

where V is the unit-cell volume, Ze is the nominal atomic charges, and δ is the atomic displacement. As all the atomic displacements occur along the c axis and there is not axial (ab-plane) contribution, the sum was calculated directly from the δ magnitudes obtained from the refinement. The obtained value is 75 μC/cm^2 for a single crystal; in a ceramic powder this value must be divided by 3. Moreover, the use of nominal charges (even though the covalency of the chemical bonds can decrease the final value of the polarization) is also an important source of errors. Another effect that reduces the experimental polarization is the presence of a dilution with the paraelectric cubic phase. Finally, we should take into account the nonsaturation conditions of the hysteresis loop, which is also indicated by the loop shape; higher fields could not be applied because of dielectric breakdown.

As temperature decreases, the magnetic correlations become stronger; Figure 10 shows the thermal evolution of the magnetic moment derived from the sequential Rietveld refinement of the magnetic structure from the D20 NPD data set. The magnetic unit cell is shown at the inset of Figure 5. It is remarkable that at room temperature there is a significant net magnetization characterized by the presence of low intensity magnetic peaks. The refined value of the magnetic moment for the Fe cations at 2 K was 4.1(3) μ_B, which is smaller than the expected value of $\mu_{eff} = 5.00$ μ_B ($S = 5/2$). At the same time, this value is in reasonable agreement with the magnetic moments of Fe found previously in magnetically ordered Pb perovskites.[28−30] As we have mentioned previously, the crystal structure of PFTW corresponds to that of a B-site disordered perovskite, in which the Fe, W and Ti cations are

dx.doi.org/10.1021/cm300470f | Chem. Mater. XXXX, XXX, XXX−XXX

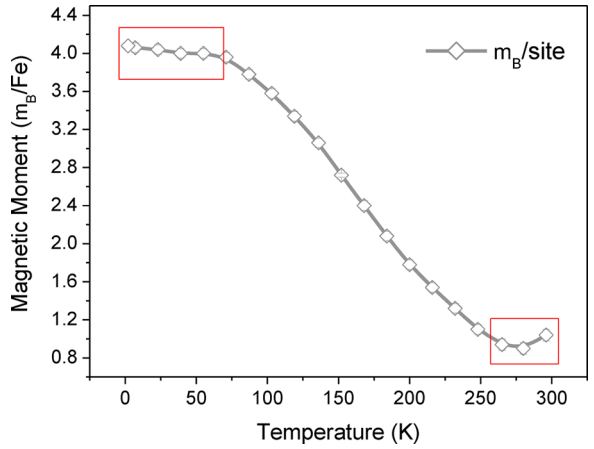

Figure 10. Thermal evolution of the ordered iron magnetic moments derived from the Rietveld refinement of the magnetic structure from NPD patterns collected from 2 to 296 K.

distributed at random in the octahedral positions. Thus, only 50% of these sites are occupied by the magnetic Fe^{3+} ions. It is likely that the strength of the antiferromagnetic interaction is severely reduced both by the disordered spatial distribution of the Fe ions and by the dilution caused by diamagnetic W and Ti cations.

By this way, the sample statistically exhibits Fe-rich islands in the bulk. They are characterized by strong antiferromagnetic interactions through Fe^{3+}−O−Fe^{3+} superexchange paths, as it occurs in $LaFeO_3$, in which the AFM ordering is reached at temperatures greater than 750 K. Additionally, a second kind of magnetic interaction is expected, given by the Fe−O−W−O−Fe and Fe−O−Ti−O−Fe super-super-exchange paths. These interactions are weaker than the Fe−O−Fe ones, so they take place at lower temperatures. Both kinds of magnetic orderings have been observed in the well-known perovskite $Pb(Fe_{2/3}W_{1/3})O_3$ (PFW),[31] which presents a completely disordered cationic distribution. This argument justifies the presence in PFTW of magnetic interactions at temperatures higher than RT, due to the strong Fe−O−Fe AFM coupling and, also, the inclusion of the second AFM super-super-exchange path at approximately 140 K, revealed by the peak in the susceptibility curve observed in Figure 7. Finally, from the magnetization curves shown at Figure 8 it is clear that the sample is not a conventional antiferromagnet. In fact, it is quite probable that the Fe-rich islands present uncompensated magnetic moments, resulting in a weak-ferromagnetic (WFM) behavior, which gives rise to a net magnetization in each island, manifested as a macroscopic magnetization of the bulk sample. Although the sample seems to be pure from the diffraction experiments, it is not possible to unambiguously assign the observed ferromagnetic response to the main phase rather than traces (below diffraction detection limit) level of iron oxide impurities. However, the presence of magnetic reflections at room temperature following the $k = [\,{}^1/_2\ {}^1/_2\ {}^1/_2\,]$ wavevector for the main phase suggests that the magnetic behavior is due to the main phase.

Chemical in-homogeneity islands might also been responsible of the distinctive features shown by the ferroelectric transition and the persistence of high-temperature cubic phase well below the transition. The scenario might be like this: islands of FE tetragonal phase would start nucleating at ∼330 K, causing the deviation from the Curie−Weiss law in the (average) paraelectric phase. The relative volume and size of these FE tetragonal phase would steadily increase on cooling until its coalescence at the transition temperature (the percentage of FE phase is close to 33% at this temperature, which is basically the percolation threshold in 3D networks). Nevertheless, islands of paraelectric phase still remain within the (average) FE phase. Whether the Fe-rich regions correspond to the initial FE nuclei or to the islands that have not still undergone the phase transition at 2 K cannot be elucidated with the available results. As said before, this behavior strongly resembles that of relaxor to ferroelectric transitions, and a major role of B-site disorder in the observed phenomenology can be assumed.

All this information is invaluable since this sample shows the coexistence of a ferroelectric and an antiferromagnetic ordering with a component of weak ferromagnetism, giving rise to a multiferroic state at temperatures very near RT. It is worth remarking that this would be an example of type I multiferroic (independent magnetic and electric orderings), among which only $BiFeO_3$ shows a higher ferroelectric transition temperature.[27] To find any interaction between both kinds of ferroic properties, we have analyzed in detail the evolution of the effective magnetic moment calculated as $\sqrt{(8\chi T)}$ and plotted as a function of temperature in Figure 7b. A careful analysis of the curve in the room temperature region shows the presence of a maximum in the magnetic moment that is centered at 300 K, approximately (see inset of Figure 7b). This event matches the development of the ferroelectric state, suggesting a correlation with the magnetic properties that can be interpreted as a magnetoelectric coupling below 300 K.

Finally, it is interesting to compare with previous results obtained for PFW,[30] a relaxor perovskite that remains cubic in the temperature range, showing a relaxor state instead of a FE transition. In PFTW the presence of the ferroactive Ti^{4+} ion seems to be responsible for the ferroelectric behavior, concomitant with the observed cubic−tetragonal transition. However, not all the material undergoes the transition at the same time, and a significant amount of cubic phase remains down to 2 K, which suggests the presence of chemical inhomogeneities. These must occur in a very small scale, for they are not unveiled by the Rietveld analysis, and they are likely related to the Fe-rich islands proposed to explain the appearance of antiferromagnetism well above room temperature. The material would develop then separated perovskite magnetic and ferroelectric phases by mechanisms similar to those taking place in relaxors. This could explain the significant magnetoelectric effect as a result of the mechanical interaction of the phases. This interaction, similarly to the case of multiferroic nanocomposites,[32] requires the piezoelectricity and magnetostriction of the phases. As much appealing as this scenario is, it is necessary to carry out a high spatial resolution structural study by advanced TEM techniques to confirm this point.

CONCLUSIONS

$Pb(Fe_{0.5}Ti_{0.25}W_{0.25})O_3$ presents a polymorphic admixture at room temperature, due to the existence of ferroelectric phase transition at $T_C \approx 293$ K. The polymorphic mixture is composed of a simple cubic perovskite belonging to the $Pm\bar{3}m$ space group (paraelectric in nature) and by a tetragonal $P4mm$ polar structure, which is isostructural to the observed for $PbTiO_3$. In both phases the B cations (Fe, Ti, W) are distributed at random on the same crystallographic sites. At

dx.doi.org/10.1021/cm300470f | Chem. Mater. XXXX, XXX, XXX−XXX

room temperature, just on the brink of the transition, the tetragonal to cubic phase ratio is 34%/66%, and it slowly increases when cooling down the sample, reaching the maximum value of 80%/20% at 2 K. The (average) paraelectric to ferroelectric transition is observed in the dielectric measurements as a sharp and intense peak in the real part of the permittivity. Moreover, we have confirmed the ferroelectric nature of the tetragonal polymorph by obtaining a hysteresis loop at 150 K. On the other hand, a weak ferromagnetic state has been observed from the magnetic susceptibility measurements, probably generated by the presence of noncompensated magnetic moments in Fe-rich islands which are a consequence of the cationic disorder in the crystal structure of the sample. Chemical heterogeneity might be also responsible of the persistence of a significant fraction of cubic paraelectric phase below the average transition temperature (~300 K). Finally, we have observed a possible magnetoelectric coupling by analyzing the thermal evolution of the effective magnetic moment, in which a peak is observed at the same temperature as the ferroelectric ordering. This is an example of near-room-temperature type I multiferroic, among which only $BiFeO_3$ shows a higher electrical ordering temperature.

■ ASSOCIATED CONTENT

Ⓢ Supporting Information

Additional figures including Rietveld refinement plot, temperature dependence, Curie−Weiss fit, and close up of NPD patterns. This material is available free of charge via the Internet at http://pubs.acs.org.

■ AUTHOR INFORMATION

Corresponding Author

*E-mail: salarreg@unsl.edu.ar.

Notes

The authors declare no competing financial interest.

■ ACKNOWLEDGMENTS

S.A.L. thanks a CONICET fellowship. J.C.P. thanks CONICET (Project PIP No. 2008-01360), SECyT-UNSL (Project PROICO 2-7707 −22/Q823). J.C.P. is a member of CONICET. J.A.A. acknowledges the financial support of the Spanish Ministry of Education to Project MAT2010-16404. The work is partially based on the results of experiments carried out at the Institut Laue-Langevin, Grenoble, France.

■ REFERENCES

(1) Hill, N. A. *J. Phys. Chem., B* **2000**, *104*, 6694.
(2) Von Hippel, A.; Breckenridge, R. G.; Chesley, F. G.; Tisza, L. *Ind. Eng. Chem. Res.* **1946**, *38*, 1097.
(3) Cohen, R. E. *J. Phys. Chem. Sol.* **2000**, *61*, 139.
(4) Bokov, A. A.; Ye, Z. G. *J. Mater. Sci.* **2006**, *41*, 31.
(5) Cohen, R. E.; Krakauer, H. *Ferroelectrics* **1992**, *136*, 95.
(6) Smolensky, G. A.; Agranovskaya, A. I.; Isupov, V. A. *Sov. Phys.—Solid State* **1959**, *1*, 149.
(7) Smolensky, G. A.; Isupov, V. A.; Krainik, N. N.; Agranovskaya, A. I. *Izv. Akad. Nauk SSR, Fiz* **1961**, *25*, 1333.
(8) Brixel, W.; Rivera, J.-P.; Steiner, A.; Schmid, H. *Ferroelectrics* **1988**, *79*, 201.
(9) Astrov, D. N.; Al'shin, B. I.; Tomashpol'skii, Y. Y.; Venevtsev, Y. N. *Sov. Phys. JETP* **1969**, *28*, 1123.
(10) Drobyshev, L. A.; Al'shin, B. I.; Tomashpolskii, Y. Y.; Venevtsev, Y. N. *Sov. Phys. Cryst.* **1970**, *14*, 634.
(11) Hill, N. A.; Filippetti, A. J. *Magn. Magn. Mater.* **2002**, *9*, 242.
(12) Seshadri, R; Hill, N. A. *Chem. Mater.* **2001**, *13*, 289.
(13) Falqui, A.; Lampis, N.; Geddo-Lehmann, A.; Pinna, G. *J. Phys. Chem. B* **2005**, *109*, 22967.
(14) Bochenek, D. *J. Alloys Compd.* **2010**, *504*, 508.
(15) Bocheneka, D.; Guzdek, P. *J. Mag. Mag. Mat.* **2011**, *323*, 369.
(16) Eiras, J. A.; Fraygola, B. M.; Garcia, D. *Key Engineering Materials* **2010**, *434*, 307.
(17) Yang, H.; Chi, Z. H.; Jiang, J. L.; Feng, W. J.; Cao, Z. E.; Xian, T.; Jin, C. Q.; Yu, R. C. *J. Alloys Compd.* **2008**, *1*, 461.
(18) Belik, A.; Furubayashi, T.; Matsushita, Y.; Tanaka, M.; Hishita, S.; Takayama-Muromachi, E. *Angew. Chem., Int. Ed.* **2009**, *48*, 6117.
(19) Bergman, J. G.; Crane, G. R.; Turner, E. H. *J. Solid State Chem.* **1977**, *21*, 127.
(20) Rodríguez-Carvajal, J. *Physica B* **1993**, *55*, 192.
(21) Lines, M. E., Glass, A. M. *Principles and Applications of Ferroelectric and Related Materials*; Clarendon Press: Oxford, 1977.
(22) Alguero, M.; Ricote, J.; Jimenez, R.; Ramos, P.; Carreaud, J.; Dkhil, B.; Kiat, J. M.; Holc, J.; Kosec, M. *Appl. Phys. Lett.* **2007**, *91*, 112905.
(23) Kobayashi, J.; Uesu, Y.; Sakemi, Y. *Phys. Rev. B* **1983**, *28*, 3866.
(24) Belik, A. A.; Iikubo, S.; Kodama, K.; Igawa, N.; Shamoto, S.; Niitaka, S.; Azuma, M.; Shimakawa, Y.; Takano, M.; Izumi, F.; Takayama Muromachi, E. *Chem. Mater.* **2006**, *18*, 798.
(25) Halasyamani, P. *Chem. Mater.* **2004**, *16*, 3586.
(26) Min, K.; Halasyamani, P. *Chem. Mater.* **2006**, *18*, 3176.
(27) Lawes, G.; Srinivasan, G. *J. Phys. D: Appl. Phys.* **2011**, *44*, 243001.
(28) Ivanov, S. A.; Eriksson, S. G.; Tellgren, R.; Rundlof, H. *Mater. Res. Bull.* **2004**, *39*, 2317.
(29) Ivanov, S. A.; Tellgren, R.; Rundlof, H.; Thomas, N. A.; Ananta, S. *J. Phys.: Condens. Matter* **2000**, *12*, 2393.
(30) Ivanov, S. A.; Eriksson, S. G.; Thomas, N. W.; Tellgren, R.; Rundlof, H. *J. Phys.: Condens. Matter* **2001**, *13*, 25.
(31) Ye, Z. G.; Toda, K.; Sato, M.; Kita, E.; Schmidt, H. *J. Korean Phys. Soc.* **1998**, *32*, S1028.
(32) Zavaliche, F.; Zheng, H.; Mohaddes-Ardabili, L; Yang, S.; Zhan, Q; Shafer, P; Reilly, E.; Chopdekar, R.; Jia, Y.; Wright, P.; Schlom, D. G.; Suzuki, Y.; Ramesh, R. *Nano Lett.* **2005**, *50*, 1793.